Optics Letters

Excitation of switching waves in normally dispersive Kerr cavities

Jonathan Lottes,[1] Gino Biondini,[1] and Stefano Trillo[2,*]

[1]Department of Mathematics, State University of New York at Buffalo, New York 14260, USA
[2]Department of Engineering, University of Ferrara, Via Saragat 1, 44122 Ferrara, Italy
*Corresponding author: stefano.trillo@unife.it

Received 22 March 2021; revised 25 April 2021; accepted 26 April 2021; posted 27 April 2021 (Doc. ID 425677); published 12 May 2021

A coherently pumped, passive cavity supports, in the normal dispersion regime, the propagation of still interlocked fronts or switching waves that form invariant localized temporal structures. We address theoretically the problem of the excitation of this type of wave packet. First, we map all the dynamical behaviors of the switching waves as a function of accessible parameters, namely, the cavity detuning and input energy deficiency, using box-like excitation of the intracavity field. Then we show how a good degree of control can be obtained by applying a negative or positive external pulsed excitation.

https://doi.org/10.1364/OL.425677

The essential features of temporal cavity solitons of coherently pumped passive Kerr resonators can be described by means of a distributed model known as the Lugiato–Lefever equation (LLE) [1,2]. The popularity of the LLE is due to its simplicity and ability to account for the cavity dynamics in both fiber loops [3,4] and microresonators [5,6]. In the anomalous dispersion regime, solitons are of the bright type with finite background and have attracted tremendous interest as bits for all-optical storage in fiber rings [3,4], and in CW-pumped high-Q microresonators as the key to form and shape highly coherent frequency combs, where the comb lines can stably lock and self-organize into an ultrashort soliton, whose Fourier transform determines the spectral envelope of the comb [7,8]. Indeed, localized LLE structures have a pivotal role in microcomb stabilization [9].

Importantly, the LLE possesses localized structures of the dark type also in the normal dispersion regime. Experimental evidence for their formation is currently being investigated in Kerr microcombs [10–15] and fiber-based resonators [16,17]. Theoretically, it is clear that such a type of localization finds its main underlying mechanism in the possibility to form bound states of frozen fronts (or switching waves as called in the pioneering work by Rozanov *et al.* [18]) that connect the coexisting upper and lower branches of the bistable steady-state response. Different theoretical aspects of this scenario have been analyzed in a number of recent papers [17,19–27]. In particular, it has been shown that the interlocking of fronts follows a complex bifurcation scenario where states of different widths coexist according to a picture known as collapsed snaking [24,25]. However, it is still not clear how the coexisting states could be selectively excited and controlled. The aim of this Letter is to analyze this aspect, starting back from the basic features of such localized waves. In particular, we show that both negative and positive pulsed excitation can be exploited, with modulation instability (MI) [2] playing a role under appropriate conditions. Such schemes are complementary to those used in microresonators, which range from the detuning sweep of the pump into a resonance where MI can be assisted by mode-coupling [11], to self-injection locking [15], or synchronous pulsed-pumping at the free-spectral range of the cavity or its harmonics.

We start from the LLE, written in dimensionless units [1,2]:

$$i\frac{\partial q}{\partial z} - \frac{1}{2}\frac{\partial^2 q}{\partial t^2} + |q|^2 q = (\delta - i)\, q + i\sqrt{p}, \tag{1}$$

where $q = q(z, t)$ is the intracavity field, and the key parameters are the cavity detuning δ and driving power p. It is well known that the steady cavity response, obtained from the LLE (1) when all derivatives are zero in the form $p = |q|^2[1 + (\delta - |q|^2)^2]$, becomes bistable for $\delta > \sqrt{3}$, giving rise to a lower branch q_- and an upper branch q_+ of CW solutions, connected by an intermediate negative-slope branch q_i that is unconditionally unstable [see Fig. 1(c)]. In this regime, traveling fronts, connecting the backgrounds q_+ to q_-, exist as solutions $q(t, z) = f(t - vz) \equiv f(\tau)$ of the ordinary differential equation $-ivf' - f''/2 + f^3 = (\delta - i) f + i\sqrt{p} = 0$, with boundaries at $f(\tau = \pm\infty) = q_\pm$ (here $f' = df/d\tau$). Such solutions exist in the range $p_{\rm lo} < p < p_{\rm hi}$, where $p = p_{\rm hi,lo}$ are the knees of the bistable response [Fig. 1(c)] given by the extrema of p as a function of $|q|^2$, located at the values $|q|^2 = \frac{1}{3}[2\delta \pm \sqrt{\delta^2 - 3}]$. We numerically computed the full family of fronts and summarized their features in Figs. 1(a), 1(b). Generally, the fronts are moving, and Fig. 1(a) shows how the velocity v depends on the parameters $(\delta, \sqrt{p})$ in the existence domain of the fronts. It is noteworthy that, for fixed detuning δ, a single value of driving power exists, which we denote as $p_o = p_o(\delta)$, such that pinning of the front occurs, yielding $v = 0$. In Fig. 1(b), we report typical profiles of the pinned fronts, sampled along the locus $p = p_o$ [thick yellow line in Fig. 1(a)]. Note also the pinned fronts are always MI stable [MI occurs only above the dashed black line in Fig. 1(a)]. Nevertheless, as we will show, MI can affect the formation of interlocked fronts. The oscillating structure of the fronts near q_- allows for a still front and its specular image to be interlocked

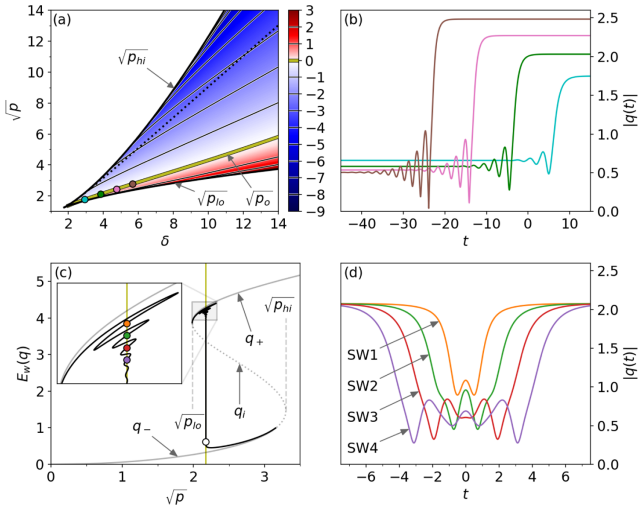

Fig. 1. (a) False color level plot with contour lines of the front velocity v in the existence domain of the parameter plane $(\delta, \sqrt{p})$ delimited by the knees of the bistable response $p_{\rm hi}$, $p_{\rm lo}$. Dotted line: MI threshold of the lower equilibrium q_-; thick yellow line: locus of pinned ($v = 0$) fronts. (b) Sampled profiles of pinned fronts corresponding to bullets of the same color in (a). (c) Bifurcation structure (inset is a zoom) of SWs for $\delta = 4$, superimposed to the stationary response. Close to the bottom, right turn of the bifurcation curve SWs becomes of the bright type: the open circle stands for the case shown in Fig. 5, right column. (d) Sampled profiles of stable SW (interlocked fronts) corresponding to bullets of the same color in (c).

to form dark bound states of different widths according to the number of interlocked oscillations [18]. Detailed studies of their bifurcation structure [24,25] show that these waves are organized in the collapsed snaking structure shown in Fig. 1(c) (obtained here through the continuation package AUTO). The profiles of these localized wave profiles are shown in Figs. 1(c) and 1(d). We label them as "switching wave" $1, 2, \ldots, n$ (or SW1, SW2, SWn for brevity) according to the order in which they are encountered in the bifurcation diagram in Fig. 1(c), i.e., in order of decreasing average energy $E_w = T_w^{-1} \int_{-T_w/2}^{T_w/2} |q|^2 \mathrm{d}t$, with T_w being a fixed measuring window (beyond which periodic boundary conditions are enforced). Generally speaking, SWn will have $2n$ local minima arising from the interlocked oscillations. The bifurcation structure implies—in the diagram E_w versus $\sqrt{p}$—successive twists of decreasing amplitude that rapidly collapse into a vertical line at $p = p_o$, which corresponds to front pinning. It turns out [25] that these waves can be stable only over the branches highlighted by the central colored circles, which in turn correspond to the profiles shown in Fig. 1(d). It is, however, not clear how the initial value problem affects the formation of one or another of these coexisting SWs.

To explore this question, we first consider the evolution of box-type initial profiles $q(t, 0)$ in which $q(t, 0) = q_-$ for $|t| < T/2$ and $q(t, 0) = q_+$ for $|t| > T/2$, where $q_\pm$ denote again the CW equilibria, and T is the temporal duration ("width") of this box-type profile. We also set $p = p_o$ in force of the collapsed snaking structure (only SW of lowest orders can exist in a finite small range around $p = p_o$). Figure 2 shows a few representative cases illustrating the possible dynamical outcomes depending on the width of the initial box-type profile, computed by numerically solving (1). When the box has a

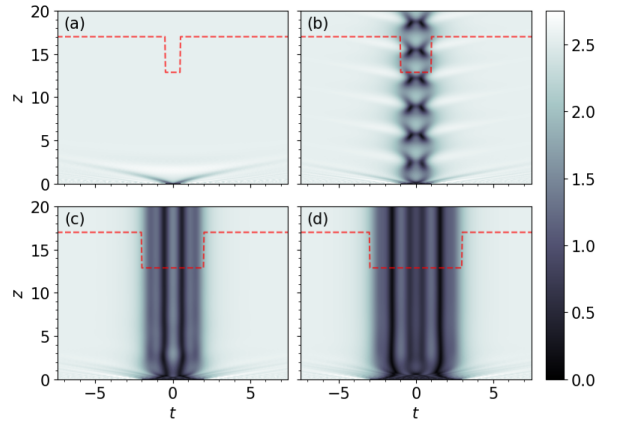

Fig. 2. Density plots showing the evolution of various box-type initial profiles (dashed red curves at the top of each panel) of duration T, with fixed $\delta = 6$ and $p = p_o$ (i.e., chosen on the curve of $v = 0$ fronts): (a) $T = 1$, resulting in decay to the uniform equilibrium state; (b) $T = 2$, resulting in an oscillatory state; (c) $T = 4$, resulting in a SW2; (d) $T = 6$, resulting in a SW3. The same color bar, shown in the panel to the right, is also used in Figs. 4 and 5.

small width, the profile decays to a stable uniform equilibrium [Fig. 2(a)]. Conversely, when the width of the initial box is sufficiently large, the profile evolves into one of the stable coexisting SWs [Figs. 2(c), 2(d)], depending on the width of the initial box-type profile. Finally, intermediate cases also exist that give rise to long-lived oscillatory structures [Fig. 2(b)].

To understand the transition from decay to switching waves as a function of the initial profile, it is convenient to introduce the "energy deficiency" of a wave profile as $\Delta E = T_w^{-1} \int_{-T_w/2}^{T_w/2} |q(t, 0) - q_+|^2 \mathrm{d}t$. Note that ΔE coincides with the deficiency in the L_2-norm. Each of the above box-type initial profiles has a particularly simple associated energy deficiency given by $\Delta E = |q_+ - q_-|^2 T$.

Figure 3 classifies the outcomes resulting from an initial box-type profile as a function of its width T, over a range of values of the detuning δ. For each value of δ, we set the pump power to the value p_o for which switching fronts with zero velocity exist (cf. Fig. 1). For each fixed value of δ, there is a clear sequence of thresholds that determines the dynamical outcome as a function of the energy deficiency of the input profile. Below the lowest threshold (pale blue region in Fig. 3), the initial profile decays into the uniform background q_+. Above this first threshold, there is a range of values of ΔE for which, in a certain range of values of δ, the initial profile evolves into a stable SW1 (pale orange region). Above this range of values, second and third thresholds exist, beyond which, for certain values of δ, the initial profile evolves, respectively, into a stable SW2 (pale green region), a stable SW3 (pale red region), and so on.

No analytical expression is available for the dependence of these threshold curves and the relative basin of attraction of the different SWs as a function of δ. However, it is possible to gain a better understanding of these thresholds by plotting the dynamical outcomes as a function of the L_1-norm deficiency (as opposed to the energy deficiency) defined as $\Delta L_1 = T_w^{-1} \int_{-T_w/2}^{T_w/2} |q(t, 0) - q_+| \mathrm{d}t$, which reduces to $\Delta L_1 = |q_+ - q_-| T$ for box-type initial profiles. As shown in Fig. 3(b), the dependence of the threshold values as a function of ΔL_1 takes on a particularly simple form, becoming just a

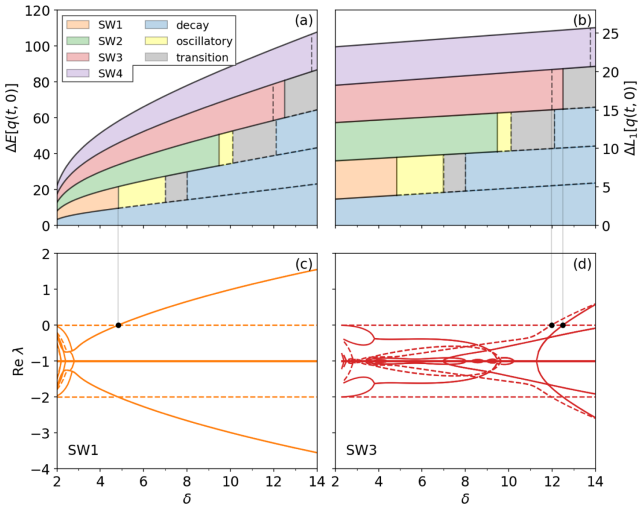

Fig. 3. Top: classification of all outcomes resulting from the evolution of initial box-type profiles in terms of its (a) energy deficiency ΔE or its (b) L_1 norm deficiency, and detuning δ. Pale orange, green, red, and purple regions give rise to a SW1, SW2, SW3, and SW4, respectively. Pale blue and yellow regions denote input profiles that decay to the uniform state q_+ or give rise to oscillatory solutions, respectively. Mixed (oscillatory or decay) behavior is found from point to point in the gray (transition) regions. Bottom: linearized spectrum of (c) SW1 and (d) SW3 profiles (solid and dashed curves stand for even and odd modes, respectively), demonstrating how the boundary of the stability regions in (a) and (b) is related to instability of even modes.

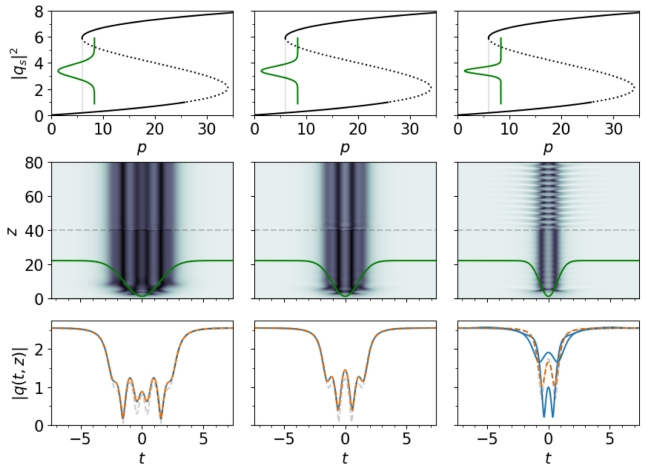

Fig. 4. Generation of SWs from steady upper branch q_+ at pump power $p_o = 8.37$ (yielding $v = 0$), for $\delta = 6$. A negative pump power pulse $p(t) = p_o - A\exp[-(t/T)^2]$, $A = 7$ is applied for $0 < z < 40$ in (1), and switched back off to $p(t) = p_o$ for $z > 40$. Top row: CW bistable response versus p (solid line indicates stable equilibria, dotted unstable) with superimposed driving pulse $p(t)$ (green). Middle row: density plots for the evolutions. The green curve again shows $p(t)$. The dashed horizontal line at $z = 40$ indicates return to CW driving at $p = p_o$. Bottom row: comparison of profiles of SW3/2/1 solutions (dashed orange curve) with $|q(t, z = 40)|$ (dashed gray curve), $|q(t, z = 80)|$ (blue curve in left/middle); the blue curves in the right panel show snapshots of the oscillatory wave with the highest and lowest minimum. Left/middle/right column: $T = 2/1.5/1$.

linear function of δ. This phenomenon has a straightforward explanation: the reason that all curves appear to collapse to the same limiting value as the detuning decreases is that in that limit, the difference $q_+ - q_-$ between the equilibria vanishes. On the other hand, the minimum box width needed to generate the various switching waves diverges in the same limit, and it does so in such a way that the product between the width and the difference between the levels varies linearly with δ, as one can see in Fig. 3(b).

Yet another feature evident in Figs. 3(a) and 3(b) is that each SW profile can be reached for values of δ only up to a certain maximum, beyond which the outcomes are either oscillations or decay to q_+. This phenomenon can be explained through a linearized stability analysis of the SW profiles. Namely, one looks for solutions in the form $q(t, z) = q_{\mathrm{sw}}(t) + \epsilon w(t, z)$, where $q_{\mathrm{sw}}(t)$ is one of the SW profiles. Inserting this ansatz into (1), keeping only terms to leading order, and writing $w(t, z) = e^{\lambda z} w_o(t)$, one obtains a linear eigenvalue problem, which can be efficiently solved numerically. The real parts of the corresponding eigenvalues are plotted in Fig. 3 for SW1 (c) and SW3 (d) as a function of δ, where dashed and solid curves correspond to eigenvalues associated with even and odd modes, respectively. Clearly, a SW is stable when all eigenvalues have negative real parts, whereas the existence of eigenvalues with a positive real part leads to instability. Indeed, Fig. 3(c) clearly shows that the boundary of the stability region for SW1 corresponds precisely to the value of δ for which the real part of one of the eigenvalues crosses zero. The situation is slightly more complicated for higher-order SWn (e.g., SW3), since in this case, both even and odd nontrivial unstable modes exist, as shown in Fig. 3(d). Since the initial profile has even symmetry, in the absence of noise, the odd mode is never excited in the dynamics, and the onset of instability is determined by the value of δ at which the first even mode reaches the instability threshold. The noise, however, could excite odd modes, hence slightly lowering the instability threshold as indicated by the dashed vertical line in Fig. 3(d).

Although the charts in Fig. 3 clarify how the stable excitation of the interlocked fronts critically depend on both the detuning and the initial width of the intracavity field excitation, in real experiments, one should rather act on the external pump p. Below we show that, starting with the cavity initially driven at a fixed detuning on a homogeneous state with constant $p = p_o$, by turning on top of it a suitable pulse shape $p(t)$ for a limited number of round trips (here in the range $0 < z < 40$), one can easily generate the localized waves with adjustable widths. Two possible scenarios involve either a negative pulse (dip) in a cavity driven on the upper branch q_+ of the bistable CW response, or a positive pulse for a cavity standing on the lower branch q_-.

Figure 4 illustrates the first scenario, with $\delta = 6$ as an example. Here we assume a negative Gaussian pulse $p(t) = p_o - A\exp[-(t/T)^2]$ (see green curves in Fig. 4), though similar results are obtained with other shapes (box, sech, etc.,). What is important is that the pulse passes the lower knee, i.e., that $A > p_o - p_{\mathrm{lo}}$ [$p_o - p_{\mathrm{lo}}$ quantifies the distance between the yellow line and the bottom boundary in Fig. 1(a) and hence is relatively small for any δ], to induce downswitching, whereas control on the generated SW can be achieved by acting only on the duration T. In particular, the longer the duration, the broader the excited SW n (or equivalently, the higher the order n). An example for $T = 2$ is reported in the left column in Fig. 4, which shows the excitation of a SW3. By decreasing the duration to $T = 1.5$, which is analogous to decreasing the input deficiency in Fig. 3, the cavity switches to

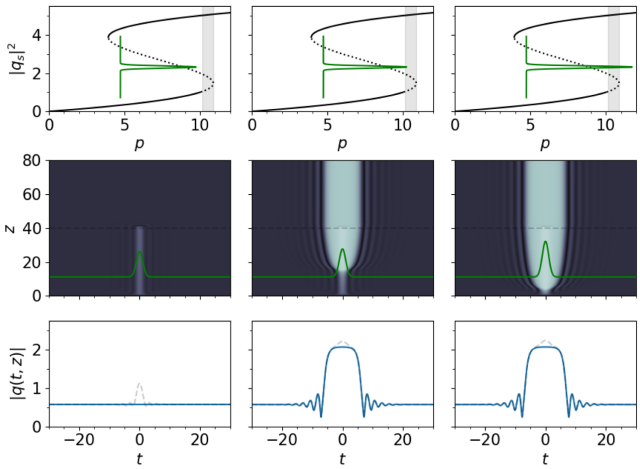

Fig. 5. Same as Fig. 4, but with $\delta = 4$ and for a positive pump power pulse $p(t) = p_o + A\exp[-(t/1.5)^2]$. The shaded region in the first row indicates MI. Left/middle/right column: $A = 5/5.5/7$.

SW2 (middle column in Fig. 4). In both cases, the long term ($z = 80$) intracavity profiles are shown to be in perfect agreement with the SW stationary solutions (see comparison between orange and blue curves in the last row of Fig. 4). However, at $\delta = 6$, Fig. 3 also suggests that lower energy deficiencies do not result in stable excitation of SW1, but rather into an oscillatory state. This is indeed what we observe by further decreasing the width to $T = 1$ (see right column in Fig. 4). Conversely, numerical simulations (not shown) indicate that the stable excitation up to the lowest branch SW 1 can be achieved at lower detunings (e.g., $\delta = 4$), again in full agreement with the results in Fig. 3.

When the cavity is set on the lower equilibrium q_-, the generation of localized waves can be induced through a positive pulse, e.g., $p(t) = p_o + A\exp[-(t/w)^2]$, whose amplitude, however, must be large enough to induce up-switching. In Fig. 5, we compare three cases with constant narrow duration ($T = 1.5$) and variable amplitude A. The left column in Fig. 5 shows the case of insufficient amplitude A, which results in simple decay. The right column shows the case where $A > p_{\mathrm{hi}} - p_o$ [the amplitude A exceeds the distance between the upper boundary and the yellow curve in Fig. 1(a)], which leads to up-switching and stable formation of a localized wave. The final profile $|q(t)|$ appears to be a narrow bright pulse with oscillating tails when referring to the central peak of $p(t)$. However, due to periodic boundary conditions, this is fully equivalent to a broad dark waveform that can be explicitly obtained by shifting the temporal window by its half width. Therefore, in this case, a narrow pulsed excitation leads to a broad SWn of high order n. Interestingly enough, in this case, the formation of localized waves can be assisted by MI. Indeed, when the peak of the driving pulse is reduced below $p_{\mathrm{hi}} - p_o$ but still above the MI threshold (dotted portion of lower branch, shaded area in the first row in Fig. 5), transient dynamics occur where it is indeed the onset of MI that drives the up-switching [26] and then the formation of the localized wave, as clearly shown by the middle column in Fig. 5.

In summary, we have discussed how the excitation of localized waves, ruled by the LLE in the normal dispersion regime, is affected by the main parameters (detuning and input deficiency). This gives important indications on the values of the parameters that lead to stable excitation of SW by means of pulsed excitation, when the cavity operates at a fixed detuning. This analysis can be extended to address extended families of localized waves that can be stabilized by higher-order dispersion [27,28]. These results will help to find alternative routes that can be implemented to realize these structures experimentally.

Funding. National Science Foundation (DMS-2009487).

Disclosures. The authors declare no conflicts of interest.

Data Availability. No data were generated or analyzed in the presented research.

REFERENCES

1. L. A. Lugiato and R. Lefever, Phys. Rev. Lett. **58**, 2209 (1987).
2. M. Haelterman, S. Trillo, and S. Wabnitz, Opt. Commun. **91**, 401 (1992).
3. F. Leo, S. Coen, P. Kockaert, L. Gelens, S.-P. Gorza, P. Emplit, and M. Haelterman, Nat. Photon. **4**, 471 (2010).
4. F. Leo, L. Gelens, P. Emplit, M. Haelterman, and S. Coen, Opt. Express **21**, 9180 (2013).
5. S. Coen, H. G. Randle, T. Sylvestre, and M. Erkintalo, Opt. Lett. **38**, 37 (2013).
6. Y. K. Chembo and C. R. Menyuk, Phys. Rev. A **87**, 053852 (2013).
7. T. Herr, V. Brasch, J. D. Jost, C. Y. Wang, N. M. Kondratiev, M. L. Gorodetsky, and T. J. Kippenberg, Nat. Photon. **8**, 145 (2014).
8. A. L. Gaeta, M. Lipson, and T. J. Kippenberg, Nat. Photon. **13**, 158 (2019).
9. P. Parra-Rivas, D. Gomila, M. A. Matias, S. Coen, and L. Gelens, Phys. Rev. A **89**, 043813 (2014).
10. W. Liang, A. A. Savchenkov, V. S. Ilchenko, D. Eliyahu, D. Seidel, A. B. Matsko, and L. Maleki, Opt. Lett. **39**, 2920 (2014).
11. X. Xue, Y. Xuan, Y. Liu, P.-H. Wang, S. Chen, J. Wang, D. E. Leaird, M. Qi, and A. M. Weiner, Nat. Photon. **9**, 594 (2015).
12. S.-W. Huang, H. Zhou, J. Yang, J. F. McMillan, A. Matsko, M. Yu, D.-L. Kwong, L. Maleki, and C. W. Wong, Phys. Rev. Lett. **114**, 053901 (2015).
13. C. Bao, Y. Xuan, C. Wang, A. Fülöp, D. E. Leaird, V. Torres-Company, M. Qi, and A. M. Weiner, Phys. Rev. Lett. **121**, 257401 (2018).
14. E. Nazemosadat, A. Fülöp, O. B. Helgason, P.-H. Wang, Y. Xuan, D. E. Leaird, M. Qi, E. Silvestre, A. M. Weiner, and V. Torres-Company, Phys. Rev. A **103**, 013513 (2021).
15. H. Wang, B. Shen, L. Wu, C. Bao, W. Jin, L. Chang, M. A. Leal, A. Feshali, M. Paniccia, J. E. Bowers, and K. Vahala, arXiv:2103.10422.
16. S. Coen, M. Tlidi, P. Emplit, and M. Haelterman, Phys. Rev. Lett. **83**, 2328 (1999).
17. B. Garbin, Y. Wang, S. G. Murdoch, G.-L. Oppo, S. Coen, and M. Erkintalo, Eur. Phys. J. D **71**, 240 (2017).
18. N. N. Rozanov, V. E. Semenov, and G. V. Khodova, Sov. J. Quantum Electron. **12**, 193 (1982).
19. A. B. Matsko, A. A. Savchenkov, and L. Maleki, Opt. Lett. **37**, 43 (2012).
20. S. Malaguti, G. Bellanca, and S. Trillo, Opt. Lett. **39**, 2475 (2014).
21. V. E. Lobanov, G. Lihachev, T. J. Kippenberg, and M. L. Gorodetsky, Opt. Express **23**, 7713 (2015).
22. V. E. Lobanov, G. Lihachev, and M. L. Gorodetsky, Europhys. Lett. **112**, 54008 (2015).
23. C. Godey, I. V. Balakireva, A. Coillet, and Y. K. Chembo, Phys. Rev. A **89**, 063814 (2014).
24. P. Parra-Rivas, D. Gomila, E. Knobloch, S. Coen, and L. Gelens, Opt. Lett. **41**, 2402 (2016).
25. P. Parra-Rivas, E. Knobloch, D. Gomila, and L. Gelens, Phys. Rev. A **93**, 063839 (2016).
26. S. Coen, M. Haelterman, P. Emplit, L. Delage, L. M. Simohamed, and F. Reynaud, J. Opt. B **1**, 36 (1999).
27. P. Parra-Rivas, D. Gomila, and L. Gelens, Phys. Rev. A **95**, 053863 (2017).
28. Z. Li, Y. Xu, S. Coen, S. G. Murdoch, and M. Erkintalo, Optica **7**, 1195 (2020).